JSST
Journal of Space Science and Technology

P-ISSN: 2008-4560
E-ISSN: 2423-4516

Journal of Space Science and Technology

Vol. 18, Special Issue, pp. 41-51, 2025
https://doi.org/10.22034/JSST.2025.1521
Journal Homepage: https://www.jsstpub.com

Original Research Paper

Numerical Study of V-Shaped Microgrooves Location on an Aerodynamic Surface for Drag Reduction

Mohammad Javad Kahalian[1], Ramin Kamali Moghadam[2]*, Iman Bahman Jahromi[3], and Mahmoud Najafi[4]

1-3. Aerospace Research Institute, Ministry of Science, Research and Technology, Tehran, Iran
4. Mathematical Science Department, Kent State University, USA

ARTICLE INFO

Article History:

Received 17 January 2025
Revised 16 February 2025
Accepted 22 February 2025
Available Online 23 February 2025

Keywords:

Microstructure
Drag reduction
Transverse flow
NACA 8-H-12

ABSTRACT

One important passive technique for drag reduction is the use of microstructured surfaces. In recent years, the advantages of this method have led some airlines to reduce their fuel consumption by installing microstructured films on aircraft. To understand the physics governing microstructures, this article investigates the effect of V-shaped transverse microgrooves on the NACA 8-H-12 airfoil. For this purpose, grooves with a base and height of 150 μm are placed transversely at eight different locations on the airfoil surface and their effects are investigated at zero angle of attack (AoA) and at velocities of 35, 65, and 100 m/s. The results show that vortices trapped within the transverse microgrooves reduce viscous drag by decreasing shear stress magnitude near the peaks and reversing its direction within the valleys. However, the microgrooves also generate pressure drag due to pressure gradients created within and around the structures. The combined effects of these changes in viscous and pressure drag determine the overall change in total drag. Total drag can either increase or decrease depending on the microgrooved surface area, its location on the airfoil, and the freestream velocity. The maximum drag reduction observed in this study was approximately 6%, achieved with two 200 mm microgrooved surfaces located mid-chord on both the suction and pressure sides at 35 m/s.

*Corresponding Author's E-mail: rkamali@ari.ac.ir

How to Cite this Article:
M. J. Kahalian, R. Kamali Moghadam, I. Bahman Jahromi, and M. Najafi, "Numerical study of V-shaped microgrooves location on an aerodynamic surface for drag reduction," *Journal of Space Science and Technology*, Vol. 18, Special Issue, pp. 41-51, 2025, https://doi.org/10.22034/JSST.2025.1521.

1. INTRODUCTION

Drag management is one of the most basic issues facing aerospace designers. While increased drag is desirable in some applications, such as reentry capsules, due to its role in energy dissipation, drag reduction is a primary concern in most aerospace designs. Microstructured surfaces [1] represent an important class of passive drag reduction techniques, which often involve manipulating surface properties such as geometry [2] and roughness [3, 4].

Walsh [5, 6, 7, 8] pioneered the study of drag reduction by ribbed surfaces. He investigated the different behavior of surfaces with bladed, scalloped and triangular riblets and showed that the symmetrical V-shaped structure had the best effect in drag reduction. Bechert et al. [9,10] investigated different configurations of bladed, scalloped, and sharkskin-like blades. They also conducted an experimental investigation into viscous reduction methods using ribbed surfaces. Djenidi and Antonia [11] measured the drag reduction effect of the V-shaped groove through experiments and found that the drag reduction effect is related to the peak-to-peak distance. Debisschop and Nieuwstadt [12] experimentally investigated the groove effect and found that in the presence of a adverse pressure gradient, the drag reduction can be as high as 13%. Duan and Choudhari [13] found by direct numerical simulation that the drag reduction mechanism proposed for incomprisible flows can still apply for high-speed boundary layers. Chu and Karniadakis [14] studied the drag reduction effect of transverse grooves under different Reynolds numbers. They found that the drag reduction was greater at higher Reynolds numbers. Ahmadi-Baloutaki et al. [15] investigated the effect of the groove surface on turbulence through experimental measurements and found that the presence of a groove increases the boundary layer thickness. Wang et al. [16] conducted a comparative study between simulation and experiment on transverse grooves and observed that a vortex structure is formed inside the transverse grooves. Sutardi and Widodo [17] evaluated the behaviour of the laminar sub-layer in a turbulent boundary using a hot-wire anemometer system. The results showed that no significant differences in the streamwise mean velocity, steamwise turbulence intensity, and velocity signals for the smooth and grooved wall cases. However, the energy spectra for the grooved wall case is slightly lower than that on the smooth wall case. The flow fields over a riblet surface with semicircular grooves were investigated using the synchronized smoke-wire method and the velocity field measurement techniques by Li and Li [18]. They studied how vortices behaved under conditions of decreasing and increasing drag, as well as the effect of the distance between the riblets and observed that if most of the streamwise vortices remained above the riblets, the flow above the riblet valley would be sufficiently calm and drag would decrease. However, if the riblet spacing was large enough that most of the streamwise vortices remained inside the riblet valley (high-velocity flows could penetrate the valleys), drag would increase.

In recent years, Guler et al. [19] used triangular riblets on the suction side of the NACA 0018 airfoil to improve its aerodynamic performance. They observed that the presence of riblet structures increased the lift coefficient and concurrently delayed the stall angle by up to 19°. Notably, the ribbed structures effectively mitigated the interaction between the laminar separation bubble and trailing-edge separation, resulting in reduced turbulent kinetic energy. Li et al. [20] used large eddy simulation (LES) to investigate the vortex structures on a ribbed surface with varying protrusion heights. They observed that the drag reduction rate increased from 3.4% when the ribs were completely submerged within the turbulent boundary layer to 7.9% when the protrusion height reached 11.2. Li et al. [21] investigated the use of transverse grooves on micro air vehicles airfoils to reduce viscous drag. By considering overall aerodynamic performance, they designed a grooved airfoil that demonstrated a 33.747% improvement in lift-to-drag ratio compared to the smooth airfoil. Pakatchian et al.'s review paper [22] is devoted to the application of riblets in the aviation industry, focusing on studies conducted in wind tunnels, flight tests, and using numerical techniques. Bliamis et al. [23] examined various blade-shaped riblet designs for use on Unmanned Aerial Vehicles. They concluded that riblets with a width-to-height ratio of 1 ($s/h = 1$) provided the best drag reduction, whereas those with the largest width ($s/h = 2$) performed poorly and exhibited exceptionally high wall shear stresses.

To elucidate the physics governing microstructured surfaces, this article investigates the aerodynamic parameters resulting from airflow over such surfaces, including drag components, velocity profiles, and shear stress. While most of the previous studies on transverse microstructures have frequently attributed drag reduction to velocity slip above the structures or a reduction in viscous drag, this work demonstrates, through analysis of shear stress distributions, that the negative viscous drag within the microgroove valleys, in addition to reduced shear stress near the peaks, contributes significantly to overall drag reduction. Furthermore, a review of the literature reveals a lack of consensus regarding the underlying physics and parametric influences of microstructures, highlighting the need for further data. Therefore, the novel aspect of this study is the investigation of V-shaped microgroove placement at various locations on an NACA 8-H-12 airfoil. Specifically, microgrooves of uniform base and height are positioned at eight distinct locations on the smooth airfoil, and the resulting drag components are analyzed at AoA = 0 and velocities of 35, 65, and 100 m/s. These results are then compared with those obtained from the smooth airfoil under identical conditions.

2. PROBLEM DEFINITION

In this section, the geometry of the airfoil and microgrooves, the locations of microgrooved surfaces on the airfoil, mesh properties, governing equations and solution method are presented. Finally, the validation of the solution method and its independence from the mesh are investigated.

2.1 Geometry and mesh

As mentioned and shown in Fig.1, V-shape transverse microgrooves with base and height of 150 µm are used in this study. These microgrooves are placed on eight different locations on the surface of the NACA 8-H-12 airfoil with chord of 220 mm, each location being identified by a unique code. Table 1 details the location of the microgrooves and corresponding case codes.

The coding system is as follows: the first part indicates on which side of the airfoil the microgrooved film is located (S for suction side, P for pressure side, SP for both); the second part indicates the film's position along the chord, relative to its center (M for symmetrical at the chord center, F for front of the airfoil, R for rear of the airfoil); and the final part represents the length of the microgrooved surface in millimeters.

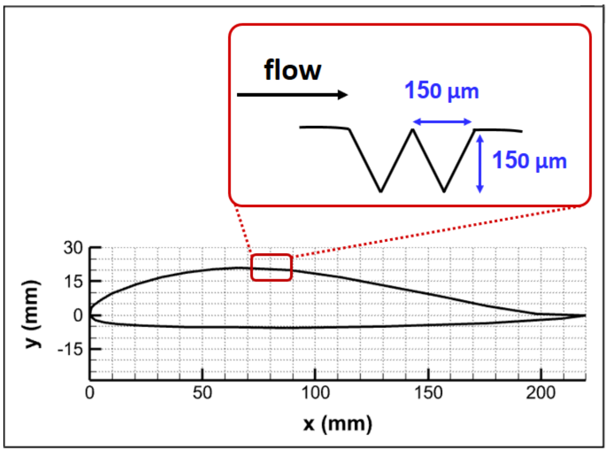

Fig. 1. Geometry of transverse microgrooves and NACA 8-H-12 airfoil.

Table 1. Location of the microgrooved surface.

Code	Location of microgrooves
SMOOTH	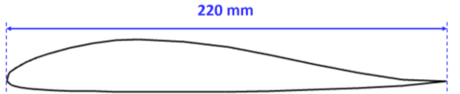
S-M-100	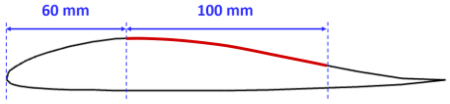
S-F-100	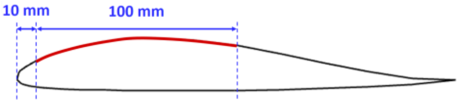
S-R-100	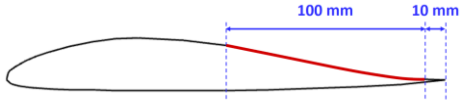
SP-F-200	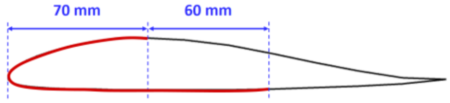
SP-R-200	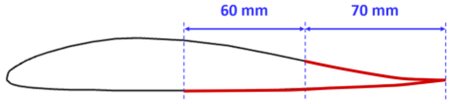
S-M-200	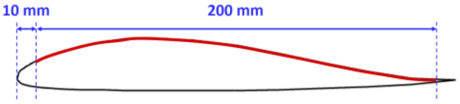
P-M-200	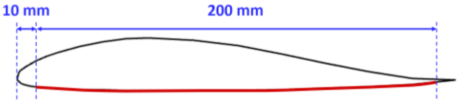
SP-M-400	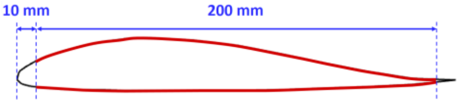

The computational domain was discretized using an unstructured mesh with several boundary layer cells. On the microgrooved surfaces, the first cell height was approximately 24 µm, with a typical cell length of 9 µm. Fig.2 presents the Y-Plus distribution of the microgrooved surface for the S-M-100 case.

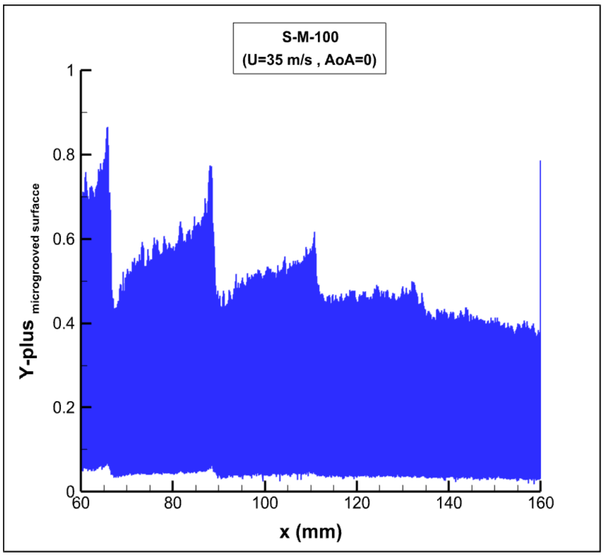

Fig. 2. Y-plus of the S-M-100 case.

2.2 Governing equations

The Knudsen number is a criterion of flow continuity that can be calculated from Eq. (1) [24].

$$Kn = \sqrt{\frac{\pi\gamma}{2}}\frac{Ma}{Re} \tag{1}$$

In this relation, γ represents the specific heat ratio, Ma the Mach number and Re the Reynolds number. Based on the size of the microgrooves, the maximum value of the Knudsen number is approximately equal to 4.3×10^{-4}; therefore considering the range of application of the Navier Stokes equations, these equations can be used in this study.

On the other hand, the primary mechanism for drag reduction in transverse microstructures is the generation of vortices within the structures, which causes local turbulence. Therefore, by using an appropriate mesh, some RANS models are able to capture local vortices and their effects. For example references [21,25,26] have also used some of these models. Considering the use of the RANS approach, the mass and momentum conservation equations are respectively [27]:

$$\frac{\partial \rho u_j}{\partial x_j} = 0 \tag{2}$$

and

$$\frac{\partial \rho u_i}{\partial t} + \frac{\partial}{\partial x_j}(\rho u_i u_j) = -\frac{\partial p}{\partial x_i} + \mu \frac{\partial^2 u_i}{\partial x_j \partial x_j} - \frac{\partial}{\partial x_j}\left(\frac{2}{3}\rho k \delta_{ij} - \mu_t\left(\frac{\partial u_i}{\partial x_j} + \frac{\partial u_j}{\partial x_i}\right)\right) \tag{3}$$

where u_i represents the average velocity vector component, p the average pressure, k the turbulence kinetic energy, δ_{ij} the Kronecker delta, μ the dynamic viscosity, and μ_t the turbulence viscosity. μ_t is calculated using turbulence models, and in this study, the k-ω SST model is employed. According to this model, the turbulence viscosity is obtained using the following relations [28, 29]:

$$\mu_t = \frac{\rho a_1 k}{max(a_1\omega\,, \sqrt{2}S_t F_2)} \tag{4}$$

In above equation, a_1 is a constant, ω is the specific turbulent dissipation rate, and S_t is the magnitude of the strain rate. k, ω, and F_2 are also calculated using the following relations:

$$\frac{\partial}{\partial t}(\rho k) + \frac{\partial}{\partial x_i}(u_i \rho k) = \frac{\partial}{\partial x_j}\left(\mu_k \frac{\partial}{\partial x_j}k\right) + \tilde{P}_k - \beta^* \rho \omega k \tag{5}$$

and

$$\frac{\partial}{\partial t}(\rho\omega) + \frac{\partial}{\partial x_i}(u_i \rho \omega) = \frac{\partial}{\partial x_j}\left(\mu_\omega \frac{\partial}{\partial x_j}\omega\right) + P_\omega - \beta\rho\omega^2 + 2\rho(1 - F_1)\frac{1}{\omega}\frac{1}{\sigma_{\omega,2}}\frac{\partial}{\partial x_j}k\frac{\partial}{\partial x_j}\omega \tag{6}$$

and

$$F_2 = tanh\left[\left[max\left(2\frac{\sqrt{k}}{\beta^*\omega(d_\perp)}, \frac{500\mu}{\rho\omega(d_\perp)^2}\right)\right]^2\right] \tag{7}$$

In these relations μ_k and μ_ω are the effective viscosities, $\tilde{P}_k$ is the effective rate of production of k, P_ω is the rate of production of ω, $d_\perp$ is the shortest distance to the near wall, β and β^* and $\sigma_{\omega,2}$ are the turbulence modeling constants, and finally F_1 is the blending function. In this study, Ansys Fluent was used to numerically solve the governing equations.

2.3 Validation of method and mesh independency

In order to validate the numerical methodology, flow over a NACA 0012 airfoil was simulated and the computed pressure and drag coefficients were compared with the experimental data reported in [30]. The airfoil chord was 67 cm, the freestream velocity is 55.35 m/s, and the AoA varied from 0° to 10°.

Figure 3 and Fig.4 show the pressure and drag coefficients, respectively. The good agreement between the present numerical results and the experimental data, as shown in these figures, validates the accuracy of the numerical methodology.

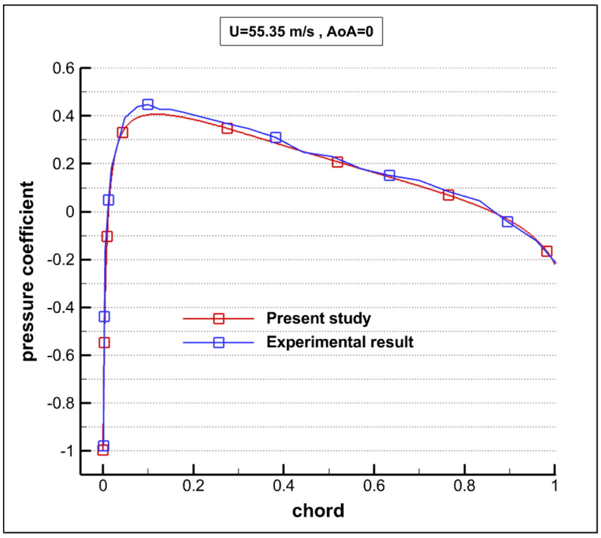

Fig. 3. Comparison of the pressure coefficients.

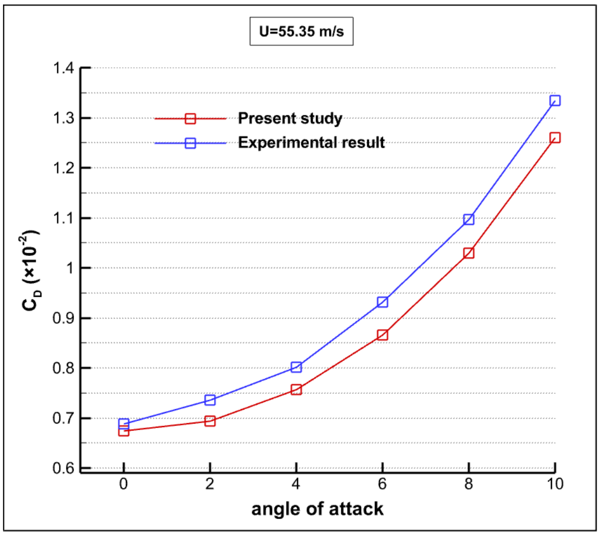

Fig. 4. Comparison of the drag coefficients.

In order to select the appropriate mesh size, four different cases were compared on the S-M-100, and finally a mesh with the mentioned specifications (section 2.1) was selected. The drag coefficients for these four cases can be seen in Fig. 5.

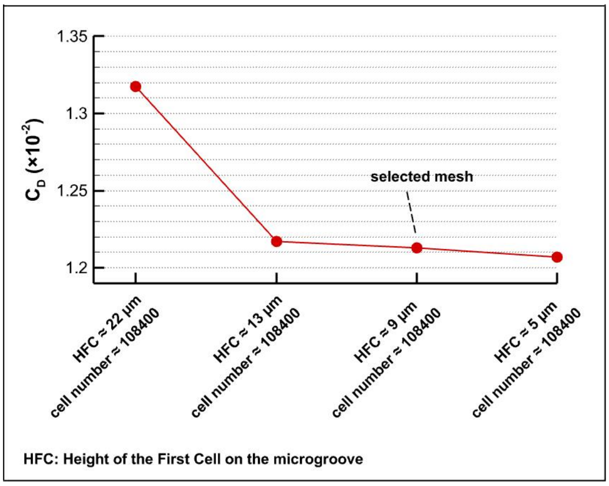

Fig. 5. Comparison of the drag coefficient, in order to investigate the independence of solution from the mesh.

3. RESULTS AND DISCUSSION

The results of this study are presented in three sections. The first section explains the mechanism by which transverse microgrooves reduce viscous drag. The second section discusses the influence of microgrooves on pressure drag generation. Finally, the third section presents the overall drag variation and the trends observed for each drag component

3.1 Mechanism of viscous drag reduction on microgrooved surface

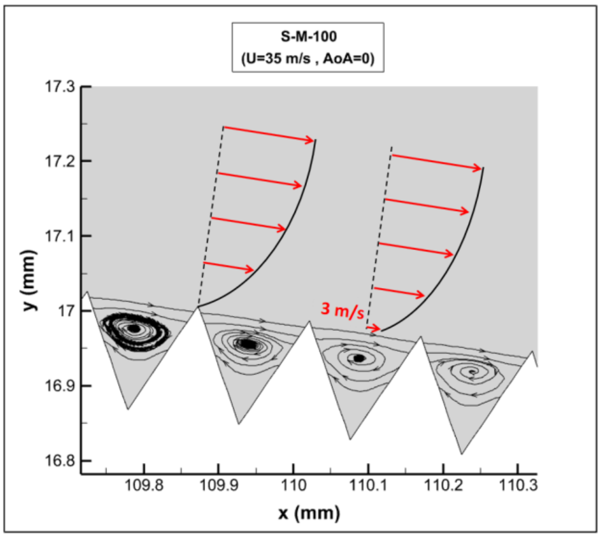

Fig. 6. Streamlines inside the microgrooves.

Figure 6 shows the streamlines for the case S-M-100 at a velocity of 35 m/s. The formation of a vortex within the microgroove causes the flow to slip over the vortex, which can be seen by comparing the profiles of velocity in Fig. 6. According to this figure, the slip velocity on the vortices in the middle of the suction side of the airfoil is approximately 3 m/s.

In describing the mechanism of viscous drag reduction, some researchers have emphasized the flow slippage on the vortex. In this article, the change in the magnitude and direction of shear stress is described as the primary mechanism of drag reduction. The equation for calculating viscous drag in the present study is [31]:

$$D_v = \int_{x_1}^{x_2} \tau_x dx \tag{8}$$

where τ_x is the shear stress in the direction of the freestream flow. Fig. **7** shows τ_x at the middle of the suction side of airfoil for the two cases of S-M-100 and smooth. In this figure, the shear stress magnitudes of the microgrooves are lower than those of the smooth surface. Furthermore, since the direction of the vortex trapped within the groove is opposite to the direction of the flow above it, the shear stress in this region becomes negative.

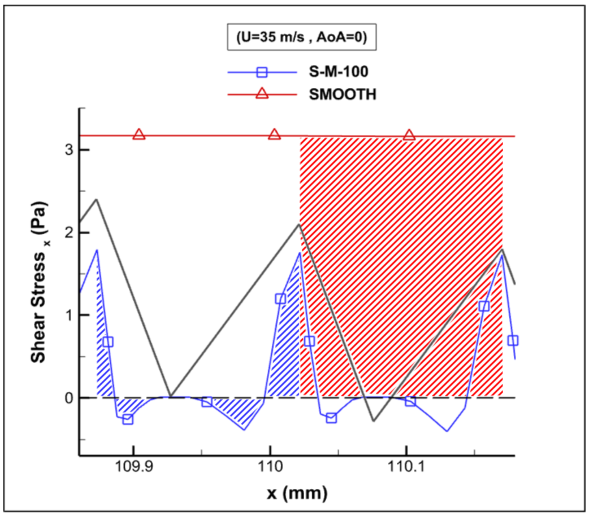

Fig. 7. Shear stress in x direction for smooth airfoil and the S-M-100 case.

According to Eq. (8), the viscous drag is calculated from the area between the graph of τ_x and the x-axis. As a result, according to Fig. 7, the decrease in the shear stress around the peak and the increase in its magnitude inside the valley (with a negative sign) leads to a decrease in the viscous drag.

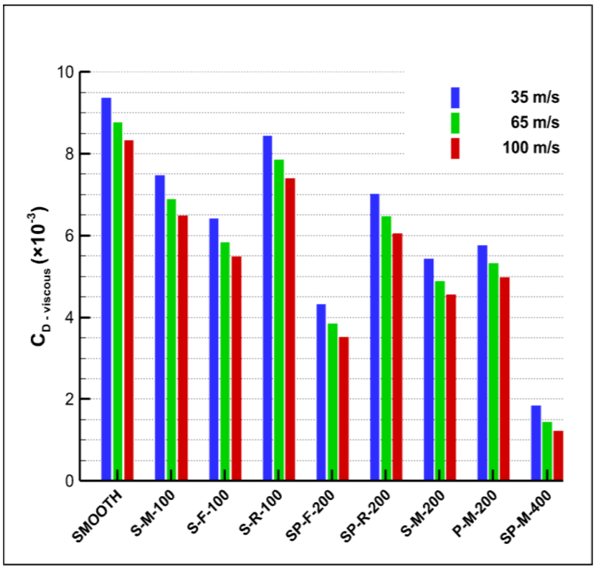

Fig. 8. Comparison of the viscous drag coefficients.

Figure 8 presents the viscous drag coefficient of different cases. According to this figure, the presence of microgrooves has reduced the viscous drag in all cases, but the amount of reduction does not depend only on the length of the microgrooved surface but also depends on its location. For example, placing 100 mm of microgrooves on the suction side and near the leading edge (S-F-100) has a greater drag reduction than placing the grooves in the middle of the airfoil (S-M-100) and also near the trailing edge (S-R-100). As another example, placing 100 mm of microgrooves on the suction side and near the leading edge (S-F-100) will reduce drag more than placing 200 mm of microgrooves around the trailing edge (SP-R-200). The trend of viscous drag reduction is similar at all three velocities, and the greatest reduction occurs in case SP-M-400.

3.2 The effect of microgrooves on the pressure drag

The use of microstructures on a smooth surface generates pressure drag, which is due to the pressure difference inside and around the structures, that ultimately creates resistance to fluid movement. Figure 9 shows the pressure difference generates around the microgrooves by comparing the static pressure on the smooth airfoil and case S-M-100.

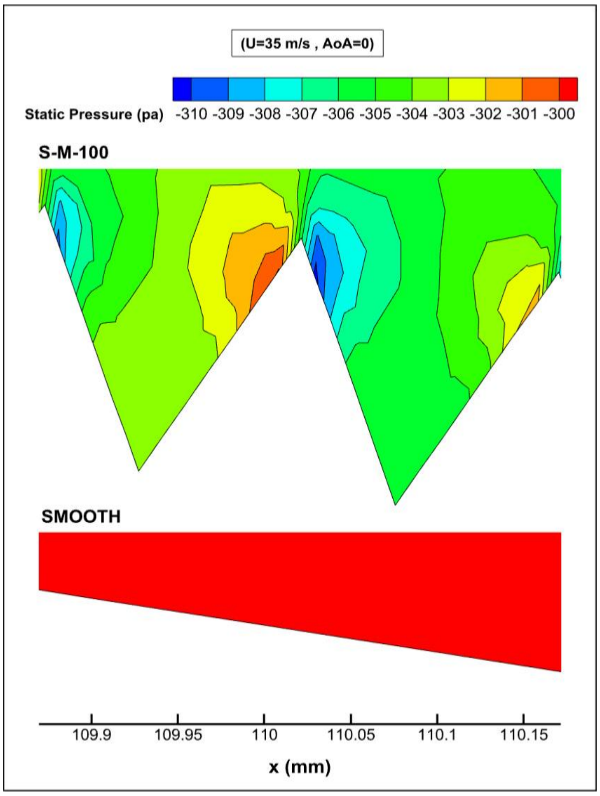

Fig. 9. Comparison of the static pressure.

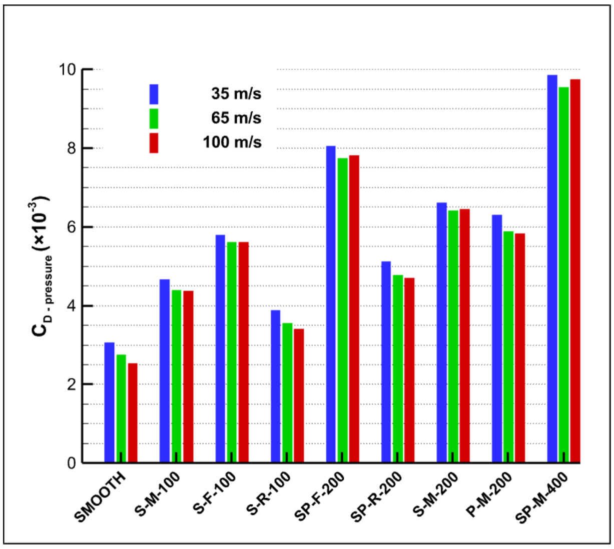

Fig. 10. Comparison of the pressure drag coefficients.

Figure 10 shows the pressure drag coefficient of different cases. In all cases, the presence of microgrooves increased the pressure drag compared to the smooth airfoil. Similar to viscous drag, the increase in pressure drag does not depend only on the length of the microgrooved surface but also depends on its location. It is noteworthy that the trend of pressure drag increase in different cases exactly follows the trend of viscous drag decrease, so that case SP-M-400, which had the largest amount of viscous drag reduction, also had the largest increase in pressure drag.

3.3 The effect of microgrooves on the total drag

The overall drag variation is determined by the combined effects of the changes in viscous and pressure drag. Figure 11 illustrates the variation of the drag components and the total drag relative to the smooth airfoil at U=35 m/s. These changes were calculated using the following equation [32].

$$\eta_t = \frac{D_{str} - D_{smh}}{D_{smh}} \times 100$$
$$= \frac{D_{str-v} - D_{smh}}{D_{smh}} \times 100 - \frac{D_{str-p}}{D_{smh}} \times 100 = \eta_v + \eta_p \tag{9}$$

Where D represents drag and η represents the percentage change relative to the smooth airfoil. The subscripts smh, str, p, v and t denote the smooth airfoil, microstructured airfoil, pressure component, viscous component, and total change, respectively.

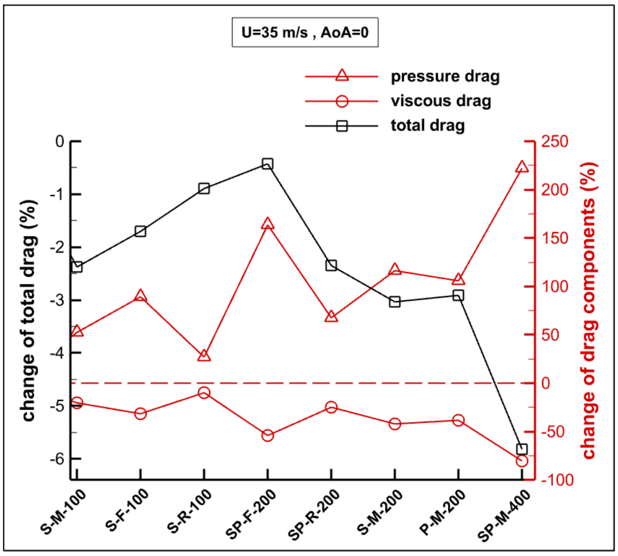

Fig. 11. The amount of change of drag components and total drag relative to the smooth airfoil.

As previously noted, the largest reduction in viscous drag occurs in case SP-M-400, which according to Fig. 11 is more than 80% (relative to the smooth airfoil). Conversely, the pressure drag increases by more than 220% (relative to the smooth airfoil). According to Fig. 12 for the smooth airfoil, the viscous component contributes approximately 75% of the total drag. Therefore, an 80% reduction in viscous drag can overcome a 220% increase in pressure drag, resulting in a total drag reduction of approximately 5%.

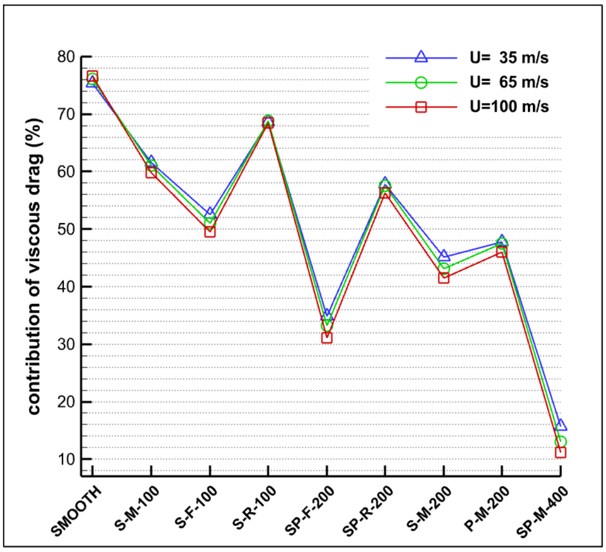

Fig. 12. Contribution of the viscous drag to the total drag.

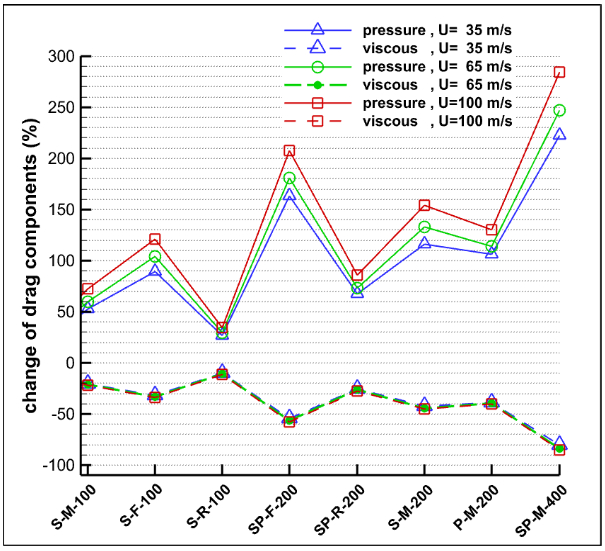

Fig. 13. The amount of change of drag components relative to the smooth airfoil at different velocities.

Figure 13 shows the change in the viscous drag and the pressure drag components of different cases at three freestream velocities of 35, 65 and 100 m/s. As can be seen, the trends in drag component variation are consistent across these velocities. Furthermore, a greater decrease in viscous drag correlates with a greater increase in pressure drag for each configuration, and these trends are consistent across all three velocities. On the other hand, in each case where the viscous drag decreases more, the pressure drag increases more, and these trends are the same for all three velocities. It is interesting to note that the trend of viscous drag change in Fig. 13 is similar to the trend of contribution in Fig. 12 In other words, a larger decrease in viscous drag is equivalent to a smaller contribution of this component to the total drag.

Figure 14 shows the variation in total drag for different cases and at freestream velocities of 35, 65 and 100 m/s. While total drag is the sum of the viscous and pressure drag components, its trend does not necessarily follow that of either component. Furthermore, despite similar trends in the variation of the drag components across the different velocities, the total drag variation differs at each velocity. As shown in Fig. 14, at 35 m/s and 65 m/s, the greatest drag reduction, approximately 6% and 4.5% respectively, is observed for the SP-M-400 case. However, at 100 m/s, the total drag for this configuration increases by approximately 1%. At this higher velocity, the greatest drag reduction, approximately 1%, is achieved by the SP-R-200. In general, a reduction in viscous drag does not guarantee a reduction in total drag. As in many cases, the use of microgrooves increased the total drag, and the amount of increase was greater at higher velocities.

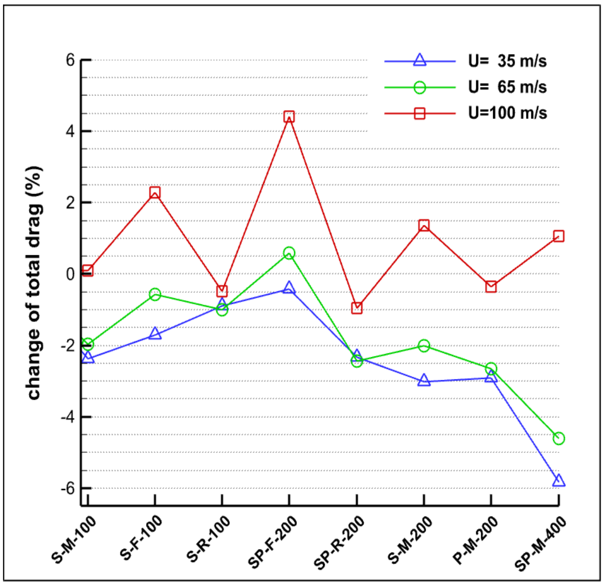

Fig. 14. The amount of change of total drag relative to the smooth airfoil at different velocities.

3.4 The effect of microgrooves on the lift

While this study focuses on drag variation, this section briefly examines the observed changes in lift. As shown in Fig. 15, across all tested velocities, placing the microstructures near the leading edge (cases S-F-100 and SP-F-200) results in a small reduction in lift (less than 1%) compared to the smooth airfoil. The two largest lift increases are observed when the microstructures are positioned near the trailing edge (cases S-R-100 and SP-R-200). For case SP-M-400, which exhibits the greatest drag reduction at 35 and 65 m/s, the change in lift is negligible, increasing by less than 1%. Conversely, case SP-R-200, which shows the greatest drag reduction at 100 m/s, also experiences the largest lift increase, approximately 3.4%.

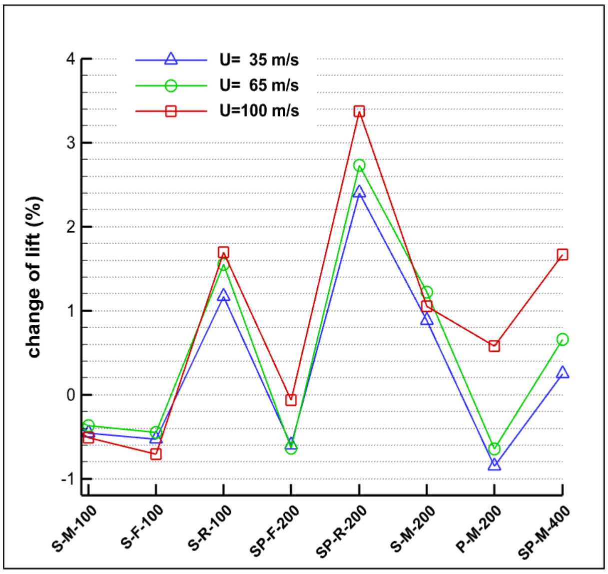

Fig. 15. The amount of change of lift relative to the smooth airfoil at different velocities.

4. CONCLUSION

This study investigates the drag reduction mechanism of V-shaped transverse microgrooves and their influence on the drag components of a NACA 8-H-12 airfoil. For this purpose, grooves with base and height of 150 μm were placed at eight different locations of the smooth airfoil with a chord of 220 mm and the drag components were investigated at AoA=0 and at velocities of 35, 65 and 100 m/s. The drag components of the microgrooved airfoils were then compared with those of the smooth airfoil under identical conditions.

The results revealed that the vortices trapped within the transverse microgrooves reduce viscous drag by decreasing the magnitude of shear stress near the peaks and altering its direction within the valleys. On the other hand, due to the pressure difference within and around the structures and ultimately the resistance to fluid movement, the use of transverse microgrooves leads to an increase in the pressure drag. The overall drag variation is then determined by the combined effects of these changes in viscous and pressure drag.

The results further indicate that the total drag can either increase or decrease depending on the microgrooved surface area, its location on the airfoil, and the freestream velocity. The maximum drag reduction observed, approximately 6%, occurred with two 200 mm microgrooved surfaces located in the mid-chord on both the suction and pressure sides at a velocity of 35 m/s.

Across the studied cases, the trend of increasing pressure drag mirrored the trend of decreasing viscous drag; the configuration exhibiting the largest decrease in viscous drag also experienced the greatest increase in pressure drag. This correlation was consistent across all three velocities (35, 65, and 100 m/s). Furthermore, the trend of the viscous component's contribution to total drag followed the same trend as the change in viscous drag itself. However, the trend in total drag variation did not necessarily align with the trends observed for either viscous or pressure drag. Total drag reduction was more prevalent at lower velocities, while at higher velocities, total drag increased in most configurations.

The AoA influences total drag by affecting its components and the flow separation point. Therefore, the increase or decrease of the drag is dependent on the AoA. Hence, a study on this relationship could be a topic for future research.

CONFLICT OF INTEREST

The authors declare that they have no conflict of interest.

REFERENCES

[1] G. D. Bixler and B. Bhushan, “Fluid drag reduction with shark-skin riblet inspired microstructured surfaces,” *Advanced Functional Materials*, vol. 23, no. 36, pp. 4507-4528, 2013, https://doi.org/10.1002/adfm.201203683.

[2] E. M. Fayyadh and N. M. Mahdi, "Effect of riblets geometry on drag reduction," in *International Mechanical Engineering Congress and Exposition. Volume 7: Fluids and Heat Transfer, Parts A, B, C, and D*, Houston, Texas, USA, 2012, pp. 87-100, https://doi.org/10.1115/IMECE2012-85228.

[3] A. C. Kah Poh, C. See Yuan, A. K. Mat Yamin, A. J. Jalaluddin, I. S. Ishak, and S. Mansor, "Effect of surface roughness on drag of loggerhead carapace," *Jurnal Mekanikal*, vol. 26, no. 2, pp. 37–48, 2018.

[4] T. S. Surwase and D. R. Vaidya, "Study of effect of surface roughness on drag," in *Mechanical Engineering PG Conference*, MAEER's MIT, United States, 2015, pp. 149–154.

[5] M. Walsh, "Turbulent boundary layer drag reduction using riblets," in *20th Aerospace Sciences Meeting*, Orlando, FL, USA, 1982, https://doi.org/10.2514/6.1982-169.

[6] M. J. Walsh, "Drag characteristics of V-groove and transverse curvature riblets," in *Symposium on Viscous Drag Reduction*, Dallas, TX, 1979, Paper 19810042106.

[7] M. J. Walsh, "Riblets as a viscous drag reduction technique," *AIAA Journal*, vol. 21, no. 4, pp. 485-486, 1983, https://doi.org/10.2514/3.60126.

[8] M. J. Walsh, "Effect of detailed surface geometry on riblet drag reduction performance," *Journal Aircraft*, vol. 27, no. 6, 1990, https://doi.org/10.2514/3.25323.

[9] D. W. Bechert, M. Bruse, and W. Hage, "Experiments with three-dimensional riblets as an idealized model of shark skin," *Experiments in Fluids*, vol. 28, no. 5, pp. 403–412, 2000, https://doi.org/10.1007/s003480050400.

[10] D. W. Bechert, M. Bruse, W. Hage, J. G. T. Van Der Hoeven, and G. Hoppe, "Experiments on drag-reducing surfaces and their optimization with an adjustable geometry," *Journal of Fluid Mechanics*, vol. 338, pp. 59–87, 1997, https://doi.org/10.1017/S0022112096004673.

[11] L. Djenidi and R. A. Antonia, "Laser Doppler anemometer measurements of turbulent boundary layer over a riblet surface," *AIAA Journal*, vol. 34, no. 5, 1996, https://doi.org/10.2514/3.13180.

[12] J. R. Debisschop and F. T. M. Nieuwstadt, "Turbulent boundary layer in an adverse pressure gradient: Effectiveness of riblets," *AIAA Journal*, vol. 34, no. 5, 1996, https://doi.org/10.2514/3.13170.

[13] L. Duan and M. Choudhari, "Effects of riblets on skin friction and heat transfer in high-speed turbulent boundary layers," in *50th AIAA Aerospace Sciences Meeting Including the New Horizons Forum and Aerospace Exposition*, Nashville, Tennessee, 2012, Paper 2012-1108, https://doi.org/10.2514/6.2012-1108.

[14] D. C. Chu and G. E. Karniadakis, "A direct numerical simulation of laminar and turbulent flow over riblet-mounted surfaces," *Journal of Fluid Mechanics*, vol. 250, pp. 1-42, 1993, https://doi.org/10.1017/S0022112093001363.

[15] M. Ahmadi Baloutaki, R. Carriveau, and D. S. K. Ting, "Effect of free-stream turbulence on flow characteristics over a transversely-grooved surface," *Experimental Thermal and Fluid Science*, vol. 51, pp. 56-70, 2013, https://doi.org/10.1016/j.expthermflusci.2013.07.001.

[16] B. Wang, J. Wang, G. Zhou, and D. Chen, "Drag Reduction by Microvortexes in Transverse Microgrooves," *Advances in Mechanical Engineering*, vol. 6, 2014, https://doi.org/10.1155/2014/734012.

[17] S. Sutardi and W. A. Widodo, "Analysis of turbulence characteristics in the laminar sub-layer region of a perturbed turbulent boundary layer," *Applied Mechanics and Materials*, vol. 836, pp. 115-120, 2016, https://doi.org/10.4028/www.scientific.net/AMM.836.115.

[18] S. J. Lee and S. H. Lee, "Flow field analysis of a turbulent boundary layer over a riblet surface," *Experiments in Fluids*, vol. 30, pp. 153–166, 2001, https://doi.org/10.1007/s003480000150.

[19] E. Güler, E. Pınar, and T. Durhasan, "The effect of riblets on the aerodynamic performance of NACA 0018 airfoil," *Cukurova University Journal of the Faculty of Engineering*, vol. 39, no. 1, pp. 119–132, 2024, https://doi.org/10.21605/cukurovaumfd.1459405.

[20] Z. LI *et al.*, "Numerical study on influence of protrusion heights on Reynolds stress and viscous stress variations in turbulent vortical structures," *Chinese Journal of Aeronautics*, vol. 37, no. 9, pp. 59-71, 2024, https://doi.org/10.1016/j.cja.2024.05.019.

[21] Z. Li *et al.*, "A numerical study on the influence of transverse grooves on the aerodynamic performance of micro air vehicles airfoils," *Applied Sciences*, vol. 13, no. 22, 2023, Art. no. 12371, https://doi.org/10.3390/app132212371.

[22] M. R. Pakatchian, J. Rocha, and L. Li, "Advances in riblets design," *Applied Sciences*, vol. 13, no. 19, 2023, Art. no. 10893, https://doi.org/10.3390/app131910893.

[23] C. Bliamis, Z. Vlahostergios, D. Misirlis, and K. Yakinthos, "Numerical simulation of blade-shaped riblets using LES based methods," *Chemical Engineering Transactions*, vol. 103, pp. 481–486, 2023, https://doi.org/10.3303/CET23103081.

[24] S. Varoutis, S. Naris, V. Hauer, C. Day, and D. Valougeorgis, "Computational and experimental study of gas flows through long channels of various cross sections in the whole range of the Knudsen number," *Journal of Vacuum Science & Technology A*, vol. 27, no. 1, pp. 89–100, 2009, https://doi.org/10.1116/1.3043463.

[25] Z. Wu, S. Li, M. Liu, S. Wang, H. Yang, and X. Liang, “Numerical research on the turbulent drag reduction mechanism of a transverse groove structure on an airfoil blade,” *Engineering Applications of Computational Fluid Mechanics*, vol. 13, no. 1, pp. 1024-1035, 2019, https://doi.org/10.1080/19942060.2019.1665101.

[26] M. E. Benhamza and F. Belaid, “Computation of turbulent channel flow with variable spacing riblets,” *Mechanika*, vol. 79 , no. 5, pp. 36–41, 2009.

[27] S. N. A. Yusof, Y. Asako, N. A. C. Sidik, S. B. Mohamed, and W. M. A. A. Japar, “A short review on RANS turbulence models,” *CFD Letters*, vol. 12, no. 11, pp. 83-96, 2020, https://doi.org/10.37934/cfdl.12.11.8396.

[28] F. Moukalled, L. Mangani, and M. Darwish, *The Finite Volume Method in Computational Fluid Dynamics*, Springer, 2016. https://doi.org/10.1007/978-3-319-16874-6.

[29] P. A. Costa Rocha, H. H. Barbosa Rocha, F. O. Moura Carneiro, M. E. Vieira da Silva, and A. V. Bueno, “K-ω SST (shear stress transport) turbulence model calibration: A case study on a small scale horizontal axis wind turbine,” *Energy*, vol. 65, pp. 412-418, 2014, https://doi.org/10.1016/j.energy.2013.11.050.

[30] N. Gregory and C. L. O’Reilly, “Low-speed aerodynamic characteristics of NACA 0012 aerofoil section, including the effects of upper-surface roughness simulating hoar frost,” AERADE Aeronautical Research Council, London, Rep. R & M. No. 3726, 1970.

[31] J. D. Anderson, *Fundamentals of Aerodynamics*, 2nd ed., McGraw-Hill Companies, 1991.

[32] Z. Li, Y. Zuo, H. Lu, L. He, and B. Meng, “Numerical study on the influence of top and valley shape of the transverse groove on the drag reduction rate,” *Journal of Theoretical and Applied Mechanics*, vol. 61, no. 4, pp. 741-754, 2023, https://doi.org/10.15632/jtam-pl/171470.